


Band offset and gap tuning of tetragonal CuO – SrTiO₃ heterojunctionsGiovanni Drera,¹ Alessio Giampietri,² Alfredo Febrari,¹ Maddalena Patrini,³ Maria Cristina Mozzati,³ and Luigi Sangaletti¹¹*I-LAMP and Dipartimento di Matematica e Fisica, Università Cattolica del Sacro Cuore via dei Musei 41, 25121 Brescia, Italy*²*Elettra-Sincrotrone Trieste, km. 163, 5-s.s.14 in Area Science Park, 34149 Basovizza, Trieste, Italy*³*Dipartimento di Fisica, Università degli Studi di Pavia, via Bassi 6, 27100 Pavia, Italy* (Received 22 June 2018; revised manuscript received 10 December 2018; published 11 February 2019)

In this work we analyze the electronic structure at the junction between a SrTiO₃ (001) single crystal and a thin tetragonal CuO layer, grown by off-axis rf sputtering. A detailed characterization of the film growth, based on atomic force microscopy and x-ray photoelectron diffraction measurements, demonstrates the epitaxial growth. We report several markers of a thickness-dependent modification of the film gap, found on both Cu 2*p* and valence band spectra; through spectroscopic ellipsometry analysis, we provide direct proof of a band gap increase in the tetragonal CuO layer (1.57 eV) with respect to the thicker monoclinic CuO layer (1.35 eV). This phenomenon is further discussed in light of cluster calculations and density functional theory + *U* simulations. Finally, we report the full experimental band junction diagram, showing a staggered configuration suitable for charge-separation applications, such as photovoltaics and photocatalysis; this configuration is observed up to very low (<3 nm) film thickness due to the gap broadening effect.

DOI: [10.1103/PhysRevB.99.075124](https://doi.org/10.1103/PhysRevB.99.075124)**I. INTRODUCTION**

The study of the peculiar properties of oxide heterostructures is a very active research topic in modern experimental physics. This renewed interest is influenced by the recent improvements in epitaxial thin-film deposition techniques, which now produce samples with unprecedented quality [1,2]. For this reason, all-oxide epitaxial heterojunctions are providing an extremely rich playground for the development of devices in the fields of spintronics, photovoltaics, and photocatalysis.

In this context, cupric oxide (CuO) shows peculiar properties both as a stand-alone material and when used in heterojunctions. In fact, CuO is the only late transition-metal (TM) monoxide to display a monoclinic unit cell in the bulk phase (hereafter denoted as m-CuO), instead of the usual cubic (rocksalt) structure. While m-CuO shows antiferromagnetism (AF), its Néel temperature T_N is considerably lower than expected (≈ 230 K) with respect to other TM oxides. However, a tetragonal CuO phase (t-CuO) has been stabilized in ultrathin epitaxial film grown on SrTiO₃ (001) [3,4] (STO). In this phase, CuO is arranged in a planar structure, with edge-sharing CuO₄ square plaquettes [shown in Figs. 1(b) and 1(c)], instead of the stripe alignment of m-CuO [Fig. 1(a)]. Calculations [5] predict t-CuO will display AF with T_N up to 900 K; moreover, a Zhang-Rice singlet dispersion similar to high- T_C cuprates was measured [6] by angle-resolved photoelectron spectroscopy (ARPES), along with a similar magnon dispersion detected by resonant inelastic x-ray scattering [7]. A suitable doping mechanism is still required to exploit a possible superconductivity, which could not be achieved by chemical means [6].

The CuO/SrTiO₃ electronic structure at the interface is also interesting; in fact, such a junction belongs to the family of all-oxide STO heterostructures, which are now actively being explored since the discovery of the two-dimensional

electron gas (2DEG) at the LaAlO₃/SrTiO₃ (LAO-STO) interface [8]. This research field has now been expanded to several perovskite and nonperovskite oxide heterojunctions [9], such as γ -Al₂O₃/STO [10], where a 2DEG has been found. In the CuO/STO system, such an effect has not yet been investigated. CuO/STO has also found important applications in photoelectrochemical water splitting; in a recent work [11], Choudhary *et al.* demonstrated that the photocatalysis performance of CuO/SrTiO₃ heterostructures is increased with respect to that of similar systems, such as Indium Tin Oxide (ITO)/STO and ITO/CuO junctions. CuO/STO also shows a superior photocurrent density and photoconversion efficiency with respect to pristine materials. In order to explain the CuO/STO photocatalysis process, a staggered band junction model was proposed, in spite of the large difference between the CuO (1.35 eV) and STO gaps (3.15 eV).

In this work, CuO thin films are grown on STO by off-axis rf sputtering, with the aim to probe the electronic properties of the junction for different thicknesses (2.7- to 42-nm range) of the CuO overlayer. This allowed us to track the transition from the m-CuO/STO to the t-CuO/STO, which we observed for a thickness below a few nanometers. In particular, the valence band alignment at the junction and the band gap broadening in t-CuO are investigated, combining indirect (x-ray photoelectron spectroscopy, XPS) and direct (spectroscopic ellipsometry, SE) experimental probes. The results are compared with bulk density functional theory (DFT) + *U* and cluster model calculations, aimed at evaluating the electronic band modification from the monoclinic to the tetragonal phase.

II. EXPERIMENTAL DETAILS

The CuO thin films were grown by rf magnetron sputtering on TiO₂-terminated STO (001) substrates, from 2-in. polycrystalline sputtering targets. In order to properly track

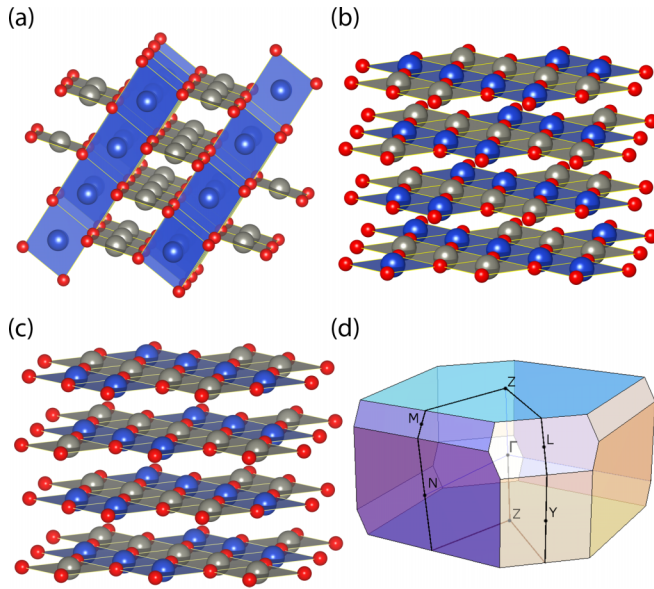


FIG. 1. Crystal structures for DFT calculation for (a) m-CuO, (b) t-CuO with rocksalt, and (c) its nearly degenerate AF order. Oxygen atoms are in red, and blue and gray indicate Cu sites with opposite spins; the planar CuO_4 plaquettes are depicted with the same color as the corresponding Cu atoms. (d) Brillouin zone for m-CuO, equivalent to the rocksalt t-CuO one.

the band shift at the interface between two insulators, we avoided the use of Nb-doped STO substrates. The sputtering power was 80 W, with an Ar flux in the 1.9–2.3-sccm range and a pressure of 8.5×10^{-3} mbar. Film crystallization was achieved with in-growth direct heating at 500°C. The STO TiO_2 termination was achieved through HF buffered solution treatment, following the method described by Koster *et al.* [12]. In order to trigger the epitaxial growth, an off-axis deposition geometry was selected, which reduces the resputtering mechanism and allows for a more homogeneous energy distribution of the deposited material [13,14]. The growth rate was approximately 0.2 Å/s. Growth morphology analysis was carried out with atomic force microscopy (AFM) in order to check the STO termination and the CuO film morphology.

The XPS analysis was performed with the $\text{Al } K_{\alpha}$ line ($h\nu = 1486.6$ eV) of a nonmonochromatized dual-anode PsP x-ray source and a VG Scienta R3000 electron analyzer operating in transmission mode. This x-ray source was adopted instead of a monochromatic one in order to mitigate the charging effects due to the insulating STO substrate; in fact, strongly focused x-ray spots, such as that of monochromatic anode sources or synchrotron radiation, lead to a strong spatial inhomogeneity of the surface charge due to the larger photon flux. Fast repeated acquisitions were performed for each spectrum in order to continuously monitor the relative peak positions, intercalated by several additional spectra on the reference C 1s peak; this methodology has been checked by the use of a flood gun and on a test growth on Nb-doped STO. The adventitious C 1s core level (Binding Energy (BE) = 284.8 eV) was used as the energy reference, leading to an overall ± 0.1 eV absolute error on the binding energy scale.

In x-ray photoelectron diffraction (XPD) measurements the angle between the x-ray direction and the analyzer axis is fixed at 55.4° . Individual XPD spectra are collected by rotating the sample polar angle θ by a 5° step, exploiting the analyzer angular mode [15], which allows for the simultaneous acquisition of XPS data in a $\pm 10^\circ$ range in the polar direction. Full stereographic images are collected by performing single XPD spectrum acquisition for various azimuthal angles ϕ in the -5° to 95° range with a step of 2.5° .

Spectroscopic ellipsometry data were measured by a VASE spectrometer by J.A. Woollam, Inc., in the spectral range from 0.5 to 5 eV at different angles of incidence from 65° to 75° . Experimental spectra were analyzed with the dedicated WVASE 32 software and database.

III. DFT+U CALCULATIONS

The electronic structure of CuO is notoriously difficult to calculate theoretically with simple *ab initio* methods due to the strong electronic correlation effects. As shown in the next section, the photoelectron spectroscopy results can be fairly predicted through a cluster model, which takes into account charge-transfer effects and core-hole interaction; however, such an approach, as in the case of model Hamiltonians ($t-J$ or Hubbard models), requires the introduction of several free parameters which must be tuned to fit the experimental data.

Conversely, a DFT, *ab initio* approach allows for the evaluation of a realistic ground-state electronic density, resulting in crystal structures which are often in good agreement with experimental results, and thus evaluation of the effect of actual Cu and O orbital geometry on the band structure.

In spite of the large number of theoretical calculations on CuO, there is still a partial disagreement about the band gap size and type (see, for instance, the review of Meyer *et al.* [16]). These discrepancies can be attributed to several reasons: the adoption of a nonprimitive unit cell, thus resulting in various Brillouin zone topologies; the choice of various AF order vectors; and different theoretical approximations [local-density approximation (LDA), LDA+ U , hybrid potentials, etc.] and computational schemes. For instance, while most experimental and theoretical works reported monoclinic CuO as an indirect band gap material [17], some authors reported a direct gap [18] or just showed a direct gap band structure plot without further specifications [19].

For these reasons, we performed *ab initio* electronic structure calculations on the CuO bulk unit cells, through density functional theory in the framework of the spin-resolved LDA-Perdew-Wang (PW) approximation [20]. Additional electronic correlation has been introduced in the LDA+ U formalism [21] since simple LDA results in a metallic ground state; several U values have been considered, namely, $U = 5$ eV, $U = 6$ eV, and the *ab initio* predicted [19] $U = 7.15$ eV.

Calculations were performed with the ABINIT package [22] in the framework of the projector augmented-wave atomic description. A $18 \times 18 \times 18$ Monkhorst-Pack grid of points in the reciprocal space and an energy cutoff of 30 hartrees for the plane-wave basis definition were used for the calculations. The m-CuO cell size was relaxed up to a maximum interatomic force of 5×10^{-6} hartrees/bohr, leading to a

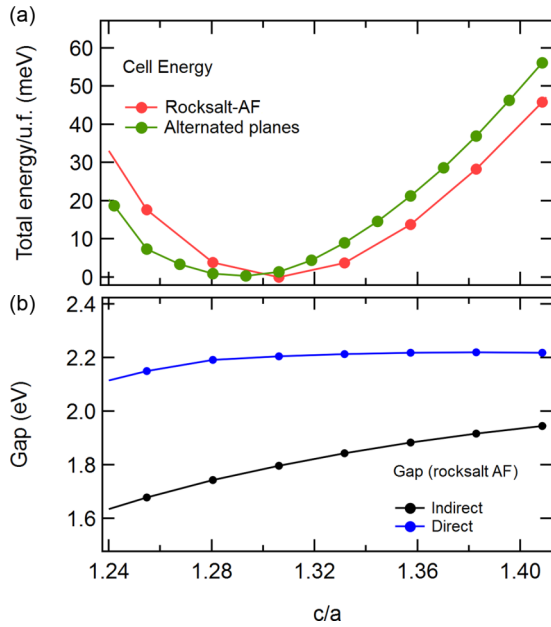


FIG. 2. (a) Calculated total energy per unit formula for the two competing AF orders of t-CuO; (b) Kohn-Sham direct (blue) and indirect (black) gaps for the rocksaltlike AF order.

small contraction (1%) of the cell parameter with respect to experimental data for any considered U value. The cell geometry and the spin order are shown in Fig. 1(a), where each CuO_4 plaquette is colored according to the spin sign. The t-CuO cell has been relaxed by keeping a fixed tetragonal base size of 3.905 Å.

For the tetragonal case, several magnetic orders have been considered. The lowest energy was found for two nearly degenerate configurations, with stripes of edge-sharing plaquettes with alternate spin in each plane, shown in Figs. 1(b) and 1(c). For $U = 7.15$ eV the total energy dependence on the c/a ratio is shown by the red and green traces in Fig. 2(a). Among the t-CuO AF configurations, the absolute lowest energy for $c/a > 1$ is a type-III AF order with $q = (1, 1, 1)$ [in cubic conventional coordinates, shown in Fig. 1(b)], which is similar to the usual rocksalt late TM-O structure. In this case, the energy minimum has been found for a tetragonal c axis equal to 5.2 Å, corresponding to $c/a = 1.33$, which is in excellent agreement with the experimental data [3]. The second-lowest-energy structure, shown in Fig. 1(c), shows a total energy per formula unit just 1 meV higher, although in this configuration the relaxed cell parameter is $c/a = 1.29$, thus lower than the experimentally observed one. The other magnetic order configurations we considered (such as horizontal and vertical CuO planes with alternated spin, not shown in this work) always result in larger total energies (with $\Delta E > 200$ meV) with different c/a ratios. Our results are similar to hybrid-functional Heyd-Scuseria-Ernzerhof (HSE)-DFT [5,23] results. Both lowest-energy AF structures show an indirect band gap and very similar spin-resolved electronic densities around Cu atoms.

We then focused on the t-CuO calculated ground state (rocksaltlike); in this case the primitive t-CuO cell becomes monoclinic ($C2/m$, space group number 12) as in the m-CuO

TABLE I. Orbital occupancy for spin-up and spin-down $3d$ orbitals of Cu atoms, as calculated by LSDA+ U with $U = 7.15$ eV. The total difference corresponds to the magnetic moment in Bohr magneton units.

	d_{xy}	d_{yz}	d_{z^2}	d_{zx}	$d_{x^2-y^2}$	Sum
m-CuO						
↑	0.947	0.935	0.904	0.937	0.981	4.704
↓	0.943	0.941	0.915	0.943	0.265	4.006
↑ - ↓	0.004	-0.006	-0.01	-0.006	0.716	0.699
t-CuO						
↑	0.948	0.940	0.932	0.940	0.973	4.734
↓	0.952	0.943	0.936	0.943	0.221	4.006
↑ - ↓	-0.004	-0.003	-0.004	-0.003	0.752	0.738

case ($C2/c$, space group number 15), with an AF magnetic order in the $(1, 0, -2)$ direction. This particular spin structure is expected only for the hypothetical bulk t-CuO; in fact, in films with a finite thickness the magnetic order can be more complex, as reported by Moser *et al.* [7]. Both t-CuO and m-CuO primitive unit cells consist of two unit formulas, with two inequivalent Cu atoms.

The $3d$ orbital occupancy, as described by the occupation matrix of the local spin-density approximation (LSDA) + U [24] in real spherical harmonics, is given in Table I for the $U = 7.15$ eV case. The average occupation of the $3d$ level for t-CuO and m-CuO is $8.7 e^-$, consistent with the expected $3d^9$ configuration of the ionic $\text{Cu}^{2+}\text{O}^{2-}$ picture. For these calculations, the CuO_2 plaquettes were oriented to have the Cu-O bond in the x -axis direction; as a result, the occupancy differences are nearly completely located on the $3d_{x^2-y^2}$ orbital. This is true even for m-CuO, where the calculated O-Cu-O angle in the plaquette plane is not exactly 90° ($\approx 83^\circ$). The spin-up and spin-down occupancy difference directly gives the magnetic moment for each Cu atom (0.70 and 0.74 Bohr magnetons for m-CuO and t-CuO, respectively, for $U = 7.15$ eV), which is consistent with other LSDA+ U calculations in the literature [17].

Indirect and direct gaps increase with the c/a ratio [Fig. 2(b)], i.e., with a larger interplanar spacing. Although from the ARPES point of view it is possible to describe the system as a set of weakly interacting planes [6], the orbital hybridization of O $2p$ with Cu d levels is thus the driving force for the gap modification. With a very relaxed geometry, the Kohn-Sham gap (listed in Table II) of t-CuO is systematically larger with respect to m-CuO for each considered U value. The calculated difference is 0.15 eV for the *ab initio* predicted $U = 7.15$. An indirect fundamental gap is always found, consistent with results in literature [17] and optical spectroscopy measurements [25] for m-CuO. At the

TABLE II. DFT+ U Kohn-Sham fundamental (indirect) and direct band gap results for m-CuO and t-CuO; all values are in eV.

U (eV)	m-CuO			t-CuO		
	5.0	6.0	7.15	5.0	6.0	7.15
Indirect gap	0.80	1.19	1.63	0.88	1.23	1.78
Direct gap	1.06	1.43	1.86	1.36	1.52	2.20

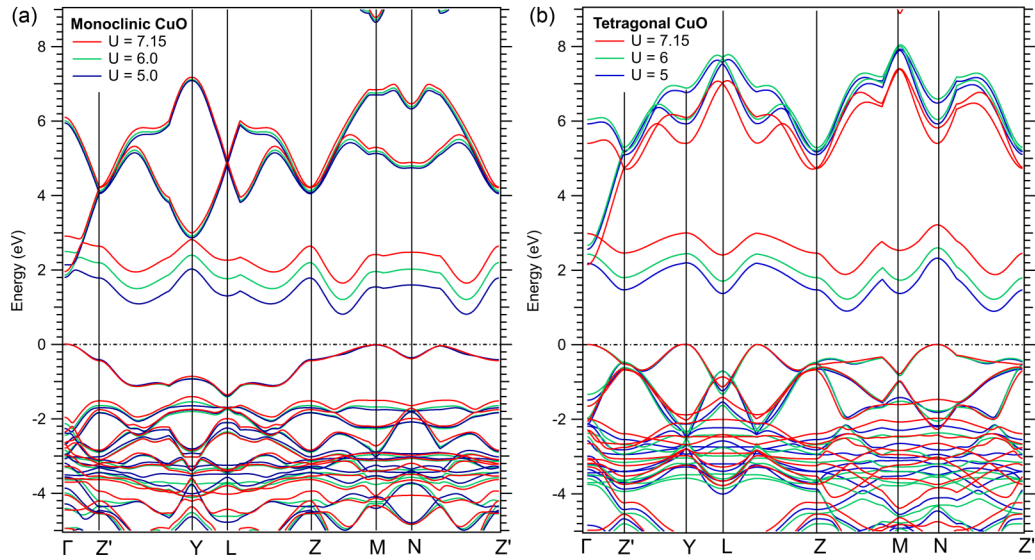


FIG. 3. Calculated DFT+ U band structures for (a) m-CuO and (b) t-CuO for different U values. The band structure path is given in Fig. 1(d).

relaxed position, the unit cell volume of t-CuO (38.885 \AA^3) is quite similar to that of m-CuO (39.251 \AA^3), as well as the in-plane plaquette bond length; we thus ascribe the gap change to the relative oxygen orbital ordering due to the different plaquette alignments. While more refined computational schemes could be applied, such as a hybrid pseudopotential or dynamical mean-field theory, DFT+ U can then describe the overall orbital reorganization of CuO in different crystal phases. In any case, these bulk crystal calculations are suitable only for adequately thick films (at least 5/6 unit cells, as in this work) since an additional gap change may occur at the interface due to the sharing of oxygen atoms between CuO and SrTiO₃, as shown by the DFT calculation by Franchini *et al.* [23]. However, in order to make these computations feasible, ferromagnetic ordering was assumed due to the high computational effort required to carry out calculations with antiferromagnetic ordering.

The detailed band structures are shown in Fig. 3; for the t-CuO case [Fig. 3(b)], the band structures were calculated with the relaxed c/a ratios, which are slightly different for each considered U . The Brillouin zone and the interpolation path for the band dispersion calculation are shown in Fig. 1(d); we choose this specific path, which covers all faces' midpoints, because it intersects with the conduction band minimum (CBM) on the Z-point centered face. The Brillouin zones of t-CuO and m-CuO are topologically equivalent. The conduction band minimum is found in a reciprocal space position which is different with respect to previous results for t-CuO (usually identified by the M point [16]). However, as already pointed out, we found several discordant results in the literature due to the adoption of a nonprimitive unit cell [26], different magnetic structures, and different notations for the band structure dispersion.

The m-projected DOS and weighted band dispersions around Cu sites are given in the Supplemental Material [27] and are compatible with the occupancy calculation results shown in Table I.

IV. EXPERIMENTS AND DISCUSSION

A. Growth characterization

In order to obtain high-quality CuO/SrTiO₃ heterostructure we initially calibrated the deposition temperature through the growth of CuO films on silicon substrates, and then we grew a set of CuO/SrTiO₃ heterostructures with different CuO film thicknesses (estimated by XPS analysis calibration). The AFM measurements on the thicker film [42 nm, labeled “thick”; Fig. 4(b)] shows the presence of a polycrystalline surface. The measured average roughness and crystal size are

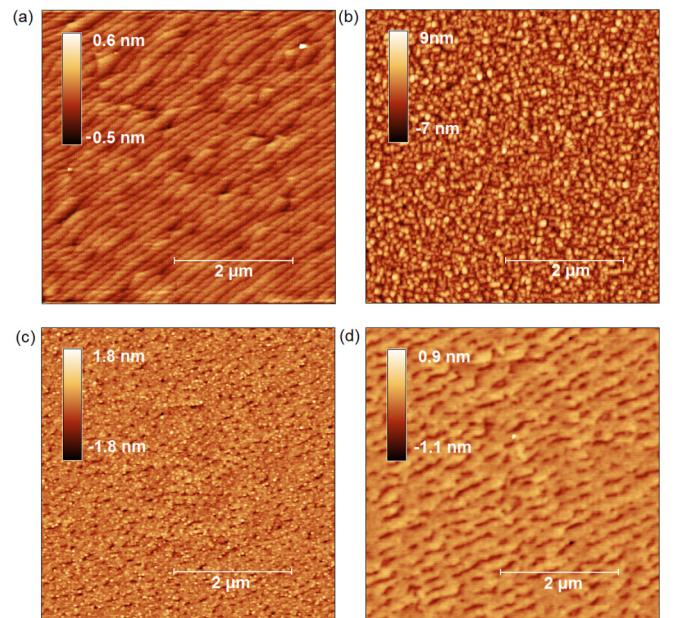


FIG. 4. AFM topographic analysis carried out on (a) the SrTiO₃ substrate and on CuO films with decreasing film thickness: (b) 42.0 nm, (c) 4.3 nm, and (d) 2.7 nm. Each image covers an area of $5 \times 5 \mu\text{m}^2$.

TABLE III. Sample list of t-CuO films grown on SrTiO₃ considered in the data analysis, with a summary of the main characterization results. Roughness and crystal size were measured by AFM; I_A , I_B , ΔE , Δ , and Q were obtained from the analysis of Cu 2*p* XPS (see text below). The band gap was measured by the SE experiment.

Label	Thickness (nm), XPS	Thickness (nm), SE	Roughness (± 0.01 nm)	Crystal size (± 0.1 nm)	I_A/I_B	ΔE (eV)	Δ (eV)	Q (eV)	Band gap, SE
Thick	42.0	40	0.85	59	2.3	8.07	1.28	8.00	1.35
Thin	4.3	4.3	0.18	11	1.9	7.81	1.43	7.98	1.44
Ultrathin	2.7	2.79	0.09		1.7	7.71	1.47	8.02	1.57

reduced for thinner films; in fact, the 4.3-nm-thick film [hereafter labeled “thin”; Fig. 4(c)] displays smaller crystals which start to displace homogeneously along the STO terraces, while an epitaxial CuO layer is obtained for the 2.7-nm-thick film [hereafter labeled “ultrathin”; Fig. 4(d)]. Indeed, due to the strong differences with respect to bulk phase, a stable t-CuO is expected only for a relatively low film thickness.

A summary of the film parameters is reported in Table III. The average roughness and crystallite average lateral size deduced from AFM are summarized. For the ultrathin (2.7-nm) sample grown on SrTiO₃ the crystal size is not reported since the film smoothly covers the SrTiO₃ terraces.

The XPS analysis confirms the stoichiometry of the grown films, and the study of the Ti 2*p* peaks (not shown here) suggests a completely oxidized Ti⁴⁺ interface, with no residual Ti³⁺ state. The XPS data have also been used to calculate the thickness (and thus the effective deposition rate) through the evaluation of Cu 3*p* and Sr 3*d* core level areas.

The epitaxial order of CuO films is probed by XPD measurements [Fig. 5(a)]. The XPD spectrum of a thick film grown on Si at 600 °C shows a featureless background, produced by the intensity attenuation of the XPS peak area on varying the tilt angle. The growth on a SrTiO₃ substrate triggers the appearance of XPD peaks, even for the thick sample, which are less intense due to the higher roughness (see Table III). This result, combined with the AFM images, demonstrates the deposition of high-quality and epitaxial CuO films by rf sputtering.

Full stereographic images were acquired both for Cu 2*p* and Sr 3*d* XPS peaks on the ultrathin film to gain information on the film and the substrate, respectively. In order to prove the crystal order, we also performed multiple-scattering simulations using the EDAC code [29] on a nearly 700 atom cluster in order to evaluate the amount of tetragonal distortion from the Cu 2*p* image [data and simulations are shown in Figs. 5(b) and 5(c), respectively]. The calculation shows nice agreement

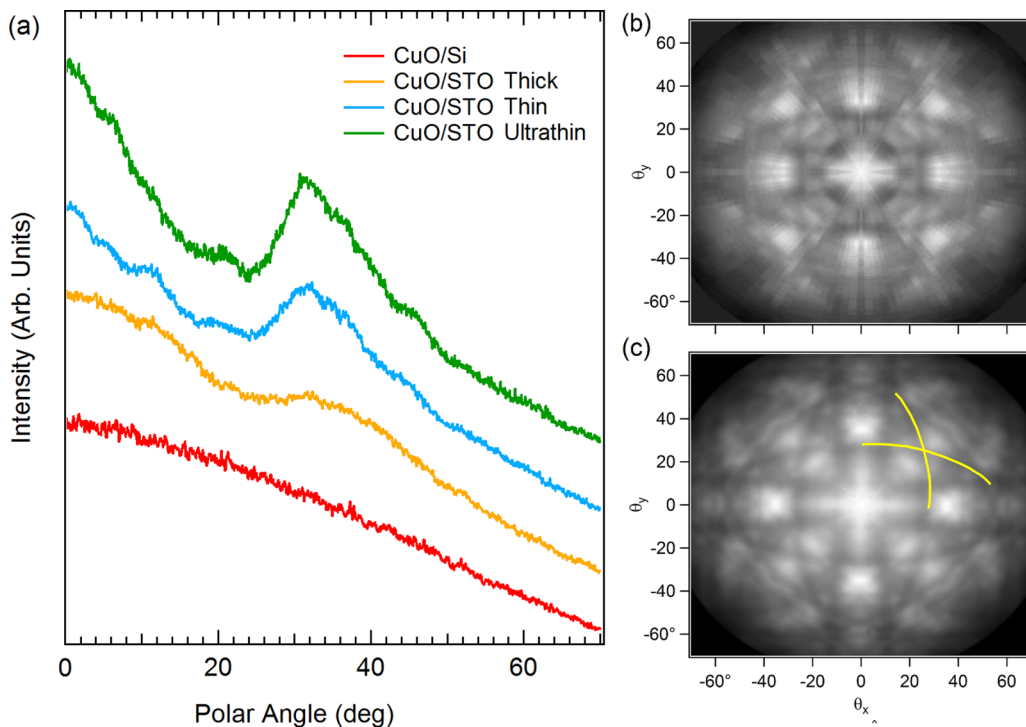


FIG. 5. (a) XPD analysis of the Cu 2*p* XPS peak area from a CuO/SrTiO₃ heterostructure for different film thicknesses. The spectra are collected by sweeping the sample polar angle in the (010) substrate plane, with a fixed azimuthal angle ($\varphi = 0^\circ$). (b) Full stereographic images obtained from the Cu 2*p* XPS peak analysis of the ultrathin film (background subtracted). (c) Multiple-scattering simulation for tetragonal Cu 2*p*, evaluated for $c/a = 1.32$.

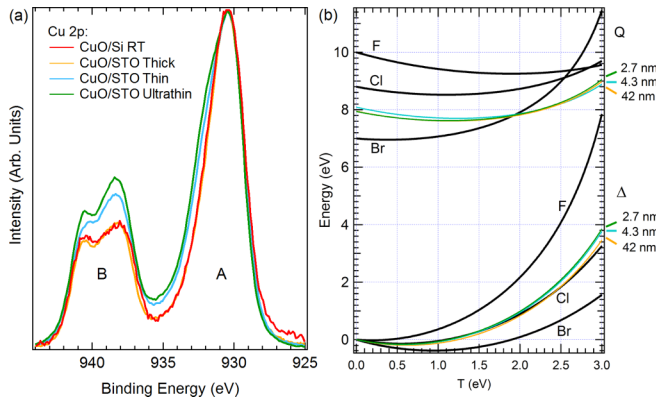


FIG. 6. (a) Cu $2p_{3/2}$ XPS peak spectra, collected from films grown on SrTiO₃ substrates with different thicknesses. For quantitative details see Table III. (b) Variation of the Coulomb interaction Q and of the energy distance between unhybridized one-hole states Δ with respect to the mixing matrix element of the Hamiltonian T , plotted using experimental values of ΔE and I_A/I_B . Values obtained from copper dihalides, plotted in black, are adapted from Ref. [28]. Values for ultrathin, thin, and thick samples are plotted in green, cyan, and orange, respectively.

with the data; in particular, the dark Kikuchi lines [highlighted in yellow in Fig. 5(c)], which cross at the position of the forward-scattering peak in the tetragonal (1,1,1) direction, are also reproduced by calculation and can be used to directly estimate a $c/a = 1.32$ ratio, in agreement with the previously reported results and with our calculations. XPD calculations for several other c/a ratios are reported in the Supplemental Material [27].

B. Electronic structure

The deposition of CuO on STO at 500 °C results in a Cu $2p$ XPS spectrum shape and peak intensity similar to those observed for a film grown on Si [Fig. 6(a)]. Along with a main line (A) at BE ≈ 930.5 eV, the Cu $2p_{3/2}$ XPS spectra show a characteristic strong satellite (B) at about 939 eV, which is absent in Cu¹⁺ and the Cu₂O compound [30]. This is a clear indication that the copper oxide films have been grown with the proper oxidation state (Cu²⁺) of the copper ion. However, the satellite intensity and its relative distance from the main line (Table III) show a clear correlation with the film thickness. Namely, the I_A/I_B intensity ratio decreases as the CuO film thickness is reduced.

The measured I_A/I_B intensity ratio and the A-B peak binding energy separation ΔE of the Cu $2p_{3/2}$ XPS spectrum can be estimated through configuration-interaction cluster model calculations, i.e., by considering an atomic Cu photoemission site within a coordination cage of oxygen atoms. In this approach, the Cu electronic structure is described as a superposition of $3d^9$ and $3d^{10} \underline{L}$ configurations, where \underline{L} represents a hole on the oxygen $2p$ orbital; the energy of each level can then be described through a limited set of parameters, such as the O $2p$ -Cu $3d$ charge transfer Δ_{CT} ; the Q_{pd} Coulomb energy, related to the interaction between the Cu $2p$ core hole created upon photoemission and the d electron in the outer shell of the Cu cation; and the T_{pd} hybridization energy

between O $2p$ and Cu $3d$ orbitals. The full description of this model can be found in the literature [28].

Using as input the experimental values of ΔE and I_A/I_B , the Q_{pd} vs T and Δ_{CT} vs T curves can be calculated, as shown in Fig. 6(b), where the curves for the present samples are added to those previously estimated by Van Der Laan *et al.* [28] for Cu dihalides and CuO. It is important to note that the T_{pd} value considered in this model should be assumed to be an effective value, as in the simple model calculations the effects of the D_{4h} symmetry on T_{pd} are not accounted for.

Unlike in the case of Cu halides our Q_{pd} curves are rather flat, but following the procedure of Ghijsen *et al.* [31], we set a common value for T_{pd} at 2.25 eV, rather similar to the T_{pd} value for bulk CuO at 2.5 eV suggested by Ghijsen *et al.* According to the Q_{pd} value we assumed, the resulting Δ_{CT} displays an overall increase of 0.2 eV (i.e., from 1.28 to 1.47 eV) as the film thickness decreases. This ordering does not change in a relatively wide range of T_{pd} energies compatible with the case of cuprates (e.g., in the 2.0–3.0 eV energy range).

Consistently, the sequence of Δ_{CT} values we report in Table III is assumed to be an indication of the overall trend of Δ_{CT} changes with thickness. As these cuprates are classified as CT insulators [32,33], the increase in charge transfer Δ_{CT} is expected to ultimately determine the increase of the energy gap, as is consistently found in the energy gap trend measured by SE (Sec. IV C) and retrieved from *ab initio* band structure calculations (Sec. III).

Further details about the m-CuO and t-CuO electronic structure can be found in the valence band (VB) photoemission spectra, shown in Fig. 7(a). In this figure, the VBs have been aligned with the Cu $3s$ core line of polycrystalline CuO in order to allow for a better comparison; please note that absolute valence band maximum (VBM) values have been obtained on VB spectra aligned with the C $1s$ reference peak. The O₁ and O₂ features correspond to the O $2s$ shallow core levels of CuO and STO, respectively; the substrate contribution cannot be detected in the thick CuO/STO due to the high overlayer thickness. The measured XPS valence band spectra, which span a 15 eV range, show a main line (A) with a shoulder on the high BE side (B) and a satellite with two features (C and D) in the 8–14 eV BE range.

The polycrystalline m-CuO spectra are consistent with the literature, while a noticeable increase in the C and B features (Fig. 7) can be detected in the heterostructures, along with a small relative shift of the uppermost energy level (A'). It should be noted that a small change in the spectral weight of the C and B components is also observed in the thick CuO/STO sample; the overall VB spectrum increase in thinner films cannot be completely justified by the presence of the STO VB contribution alone, which in any case would raise the photoelectron intensity only at the B position [see also Fig. 9(a) below].

As for the case of the $2p$ levels, the CuO valence band spectrum can be predicted with a configurational-interaction cluster-model calculation [34,35] by considering the crystal-field effect in a distorted octahedral environment (D_{4h} symmetry). Figure 7(b) shows the calculation results for several parameters, chosen to mimic a band gap increase from 1.2 to 2.4 eV, as outlined in Table II of Ref. [34]. The blue

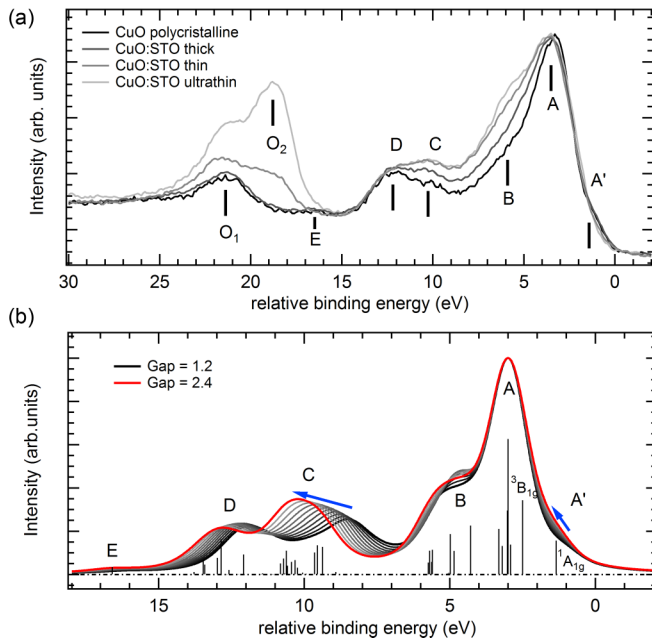


FIG. 7. (a) Experimental valence band spectra (lighter color is associated with thinner films); spectra have been aligned to the Cu $3s$ contribution of polycrystalline spectra for a better comparison. (b) Calculated VB spectra from the cluster model (described in Ref. [34]) for various band gaps. Bars refer to the case of $E_g = 2.4$ eV.

arrows point out the major changes in spectral weight with the increasing band gap, which follows the same trend as the experimental spectra. In fact, as the energy gap increases from 1.2 to 2.4 eV, the calculations show an increase in the B and C structures, along with a slight reduction in the A' shoulder. This feature was related to the Zhang-Rice singlet (see, e.g., Refs. [36,37] and references therein) and was recently mapped by ARPES [6]. The present results show that the A' feature, labeled as the $^1A_{1g}$ singlet state according to the D_{4h} cluster calculation, moves towards the second-lowest-lying state ($^3B_{1g}$ symmetry) as the band gap increases. The changes in the spectral weight in the VB region (especially the C and A' features) with respect to m-CuO were also evidenced [35] in CuGeO_3 and Bi_2CuO_4 and are mainly related to changes in the charge-transfer energy.

C. Band alignment and spectroscopic ellipsometry

In order to obtain the conduction band minimum positions, the value of the band gap must be added to the VBM calculated from the XPS data; however, the reported values for the CuO gap can vary in the 1.35–1.7 eV range [26] for both experimental and theoretical data. We then resorted to spectroscopic ellipsometry to directly probe the t-CuO gap.

In general, the ellipsometric analysis allows [38] us (i) to determine the dielectric function spectra of the film by best fitting simulated spectra to the experimental ones, (ii) to verify the correspondence between nominal and actual film thickness values, and (iii) to check the optical quality and uniformity of the films.

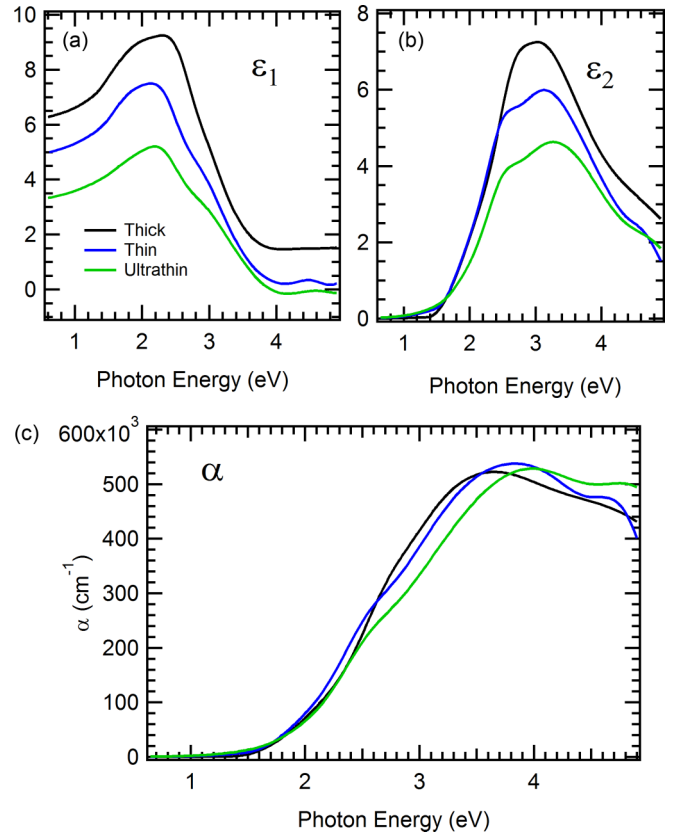


FIG. 8. The complex dielectric function ϵ components (a) ϵ_1 and (b) ϵ_2 of the CuO films as evaluated from SE. (c) Absorption coefficient measured on the CuO/SrTiO₃ samples.

First, we characterized the dielectric function of the SrTiO₃ substrate, which was in a good agreement with the database data. Then, the thin-film samples were analyzed, adopting a three-phase model made of ambient, CuO film, and SrTiO₃. The complex dielectric function $\epsilon = \epsilon_1 + i\epsilon_2$ [with $\epsilon = (n + ik)^2$, where n is the refractive index and k is the extinction coefficient] of the CuO films was first argued from numerical inversion of SE data adopting the nominal film thicknesses, as provided by XPS analysis and growth rate estimation. The resulting values for the absorption coefficient α ($\alpha = 4\pi k/\lambda$) indicate that the penetration depth of light in the film reaches tens of nanometers, so that the three-phase model has three unknown parameters: ϵ_1 , ϵ_2 , and the CuO thickness d .

We then performed a best fit of the simulated spectra to the experimental ones. We modeled the dielectric function of CuO films with Tauc-Lorentz [39] and Gaussian oscillators and obtained best-fit d values. The agreement between experimental and fitted spectra is very good, and Kramers-Kronig consistency is guaranteed by the use of physical oscillators. Moreover, the actual thickness values are within 5% of the nominal ones, as shown in Table III.

The dielectric function and absorption coefficient spectra (Fig. 8) slightly change with the film thickness, being somehow different for the ultrathin sample. This behavior is, however, compatible with the few material literature data and probably depends on the surface conditions. The Tauc $(\alpha E)^{0.5}$ plots, given in the Supplemental Material [27], display a

linear behavior which is consistent with the calculated gap values and with an indirect gap [40]. Although the nature of the band gap is still the subject of some debate [16], in the present case we have determined for the thick sample a 1.35 eV gap, in accordance with both experimental [41] and theoretical studies [42]. With decreasing film thickness the band gap energy increases by 0.2 eV (i.e., to 1.57 eV), consistent with the previous XPS analysis; SE gap results are given in Table III.

The measured indirect gap values are, in any case, lower than our calculated DFT+ U results for $U = 7.15$ eV. Apart from the known limitations of DFT for gap calculations, such a discrepancy could also be due to the strong electron-phonon coupling of CuO, which causes the reduction of the band gap as the temperature increases. Such a phenomenon has been observed in temperature-variable absorption measurements in Marabelli *et al.* [25], showing the trailing edge of absorbance data scaling down with the temperature; in that work, the gap values of 1.67 eV (consistent with ground-state DFT+ U calculation) resulted in an absorbance trailing edge of nearly 1.35 eV (consistent with our experimental data) at room temperature due to strong electron-phonon coupling.

Finally, the XPS-derived band alignment at the CuO/SrTiO₃ interfaces is shown. The STO VBMs are obtained (for low CuO thickness) by fitting the valence band spectrum of the heterojunction with the linear combination of the spectra characteristic of pristine parent compounds [9], which allows for accurate alignment of their relative energy position [Fig. 9(a)]. In particular, the shallow core levels at BE ≈ 20 eV have been used to accurately pinpoint the relative position of CuO and the STO contribution in the junction [black line in Fig. 9(a)]. The CuO VBM can be directly evaluated from the data, shown in the actual binding energy scale in Fig. 9(b); a shift towards high BE is clearly detectable for thinner CuO films. As already pointed out, some limitations to this method come from the different VB shapes for CuO due to the different electronic structures of t-CuO and m-CuO. Combined with the intrinsic difficulties in accurately determining the VBM, the leading-edge position displays an uncertainty of ± 0.15 eV, consistent with the evaluation shown by Chambers *et al.* [43] for this method. The experimentally measured band schematics for heterostructures and separated precursors are shown in Fig. 9(c).

By using the measured values, the band alignments for the thick and thin films are thus characterized by a staggered, type-II interface [Fig. 9(b)]; in such a configuration, a charge confinement within the SrTiO₃ substrate could be possible, although t-CuO is a nonpolar solid in the (001) direction. By considering the 1.35 eV gap of m-CuO, in the ultrathin case a type-I junction would be expected [red dashed line in Fig. 9(c)]. However, with the measured 0.2 eV band gap increase, the junction changes into the type-II configuration as well. By considering the gap temperature dependence [25], the conduction band displacement is expected to significantly increase at lower temperatures.

With respect to the polycrystalline sample, the CuO VBM is shifted away from the Fermi level, up to 1.2 eV for the ultrathin case. This shift, which corresponds to n -type doping, is rather unusual for CuO, which is usually considered analogous to the p -type semiconductor. A strong shift of the

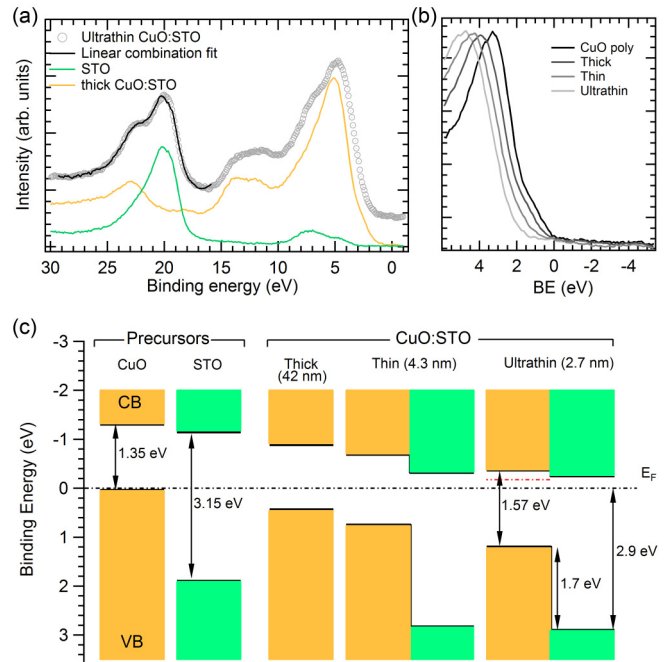


FIG. 9. XPS analysis of the band alignment. (a) Linear combination of the CuO and SrTiO₃ signals (green and yellow, respectively), which produces the fit (black line) of the signal of the CuO/SrTiO₃ heterointerface. (b) Detail of the VBMs of all heterostructures and polycrystalline CuO. (c) Schematic band alignment results for heterostructures and for the bare CuO and STO precursor. For the ultrathin film case, the position CBM evaluated from the bulk m-CuO bands is reported for comparison (red dashed lines). The band gap values for CuO were obtained with SE measurements.

STO bands towards the Fermi level with respect to the clean STO (001) surface is also observed, similar to the one reported for other perovskite-based heterostructures [44]. This shift is usually related to a strong n -type doping in STO, which in turn can be related to the presence of charge in STO whenever the band bending produces structures which cross the Fermi level. However, by considering the ultrathin case, the nearly zero conduction band offset at the CuO/SrTiO₃ junction is not compatible with an electron charge transfer in a preferential direction, at odds with other SrTiO₃-based heterostructures where a large conduction band offset usually leads to a strong charge confinement within the substrate [9].

The experimental junction diagram is then compatible with any charge-separation application (such as photovoltaics and photocatalysis), down to a few-unit-cell thickness; in particular, these results are in very good agreement with the proposed diagram for the enhanced photoelectrochemical water splitting [11] already observed in CuO/STO heterostructures.

V. CONCLUSIONS

In conclusion, several epitaxial CuO thin films were grown on SrTiO₃ by rf sputtering and were characterized by AFM, XPD, and SE analysis. Photoelectron spectroscopies (XPS and XPD) revealed the presence of CuO films with the proper stoichiometry, a nominal oxidation state of the Ti atoms in the substrate, and the clear presence of the t-CuO phase in ultrathin films. A direct measure of the band gap of CuO

allowed us to reconstruct the band alignment at the interface. XPS and SE measurements are consistent with a gap increase of 0.2 eV in t-CuO (2.7 nm), leading to a type-II junction instead of type I. Upon excitation, the conduction band offset in the CuO/SrTiO₃ junction suggests a confinement of mobile

charges (electrons) within the CuO film. Additionally, a strong shift of the Fermi level towards the CBM as a function of film thickness was measured. For all the studied films an indirect band gap is observed; the gap type and broadening results are also consistent with DFT+*U* calculations.

-
- [1] G. Koster, M. Huijben, and G. Rijnders, *Epitaxial Growth of Complex Metal Oxides* (Woodhead Publishing, Cambridge, UK, 2015).
- [2] D. Samala and G. Koster, *J. Mater. Res.* **30**, 463 (2015).
- [3] W. Siemons, G. Koster, D. H. A. Blank, R. H. Hammond, T. H. Geballe, and M. R. Beasley, *Phys. Rev. B* **79**, 195122 (2009).
- [4] D. Samal, H. Tan, Y. Takamura, W. Siemons, J. Verbeeck, G. Van Tendeloo, E. Arenholz, C. A. Jenkins, G. Rijnders, and G. Koster, *Europhys. Lett.* **105**, 17003 (2014).
- [5] X.-Q. Chen, C. L. Fu, C. Franchini, and R. Podloucky, *Phys. Rev. B* **80**, 094527 (2009).
- [6] S. Moser, L. Moreschini, H.-Y. Yang, D. Innocenti, F. Fuchs, N. H. Hansen, Y. J. Chang, K. S. Kim, A. L. Walter, A. Bostwick, E. Rotenberg, F. Mila, and M. Grioni, *Phys. Rev. Lett.* **113**, 187001 (2014).
- [7] S. Moser, N. E. Shaik, D. Samal, S. Fatale, B. Dalla Piazza, M. Dantz, J. Pellicciari, P. Olalde-Velasco, T. Schmitt, G. Koster, F. Mila, H. M. Rønnow, and M. Grioni, *Phys. Rev. B* **92**, 140404(R) (2015).
- [8] A. Ohtomo and H. Y. Hwang, *Nature (London)* **427**, 423 (2004).
- [9] A. Giampietri, G. Drera, and L. Sangaletti, *Adv. Mater. Interfaces* **4**, 1700144 (2017).
- [10] P. Schütz, F. Pfaff, P. Scheiderer, Y. Z. Chen, N. Pryds, M. Gorgoi, M. Sing, and R. Claessen, *Phys. Rev. B* **91**, 165118 (2015).
- [11] S. Choudhary, A. Solanki, S. Upadhyay, N. Singh, V. R. Satsangi, R. Shrivastav, and S. Dass, *J. Solid State Electrochem.* **17**, 2531 (2013).
- [12] G. Koster, B. L. Kropman, G. J. H. M. Rijnders, D. H. A. Blank, and H. Rogalla, *Appl. Phys. Lett.* **73**, 2920 (1998).
- [13] R. R. Das, D. M. Kim, S. H. Baek, C. B. Eom, F. Zavaliche, S. Y. Yang, R. Ramesh, Y. B. Chen, X. Q. Pan, X. Ke, M. S. Rzechowski, and S. K. Streiffer, *Appl. Phys. Lett.* **88**, 242904 (2006).
- [14] S. H. Baek, H. W. Jang, C. M. Folkman, Y. Li, B. Winchester, J. X. Zhang, Q. He, Y. H. Chu, C. Nelson, M. S. Rzechowski, X. Q. Pan, R. Ramesh, L. Q. Chen, and C. B. Eom, *Nat. Mater.* **9**, 309 (2010).
- [15] G. Drera, G. Salvinelli, J. Ahlund, P. G. Karlsson, B. Wannberg, E. Magnano, S. Nappini, and L. Sangaletti, *J. Electron Spectrosc. Relat. Phenom.* **195**, 109 (2014).
- [16] B. K. Meyer *et al.*, *Phys. Status Solidi B* **249**, 1487 (2012).
- [17] Y. Wang, S. Lany, J. Ghanbaja, Y. Fagot-Revurat, Y. P. Chen, F. Soldera, D. Horwat, F. Mücklich, and J. F. Pierson, *Phys. Rev. B* **94**, 245418 (2016).
- [18] T. Ito, H. Yamaguchi, T. Masumi, and S. Adachi, *J. Phys. Soc. Jpn.* **67**, 3304 (1998).
- [19] C. E. Ekuma, V. I. Anisimov, J. Moreno, and M. Jarrell, *Eur. Phys. J. B* **87**, 23 (2014).
- [20] M. Marques, M. Oliverira, and T. Burnus, *Computer Phys. Commun.* **183**, 2272 (2012).
- [21] B. Amadon, F. Jollet, and M. Torrent, *Phys. Rev. B* **77**, 155104 (2008).
- [22] X. Gonze *et al.*, *Comput. Phys. Commun.* **205**, 106 (2016).
- [23] C. Franchini, X. Chen, and R. Podloucky, *J. Phys.: Condens. Matter* **23**, 045004 (2011).
- [24] A. I. Liechtenstein, V. I. Anisimov, and J. Zaanen, *Phys. Rev. B* **52**, R5467 (1995).
- [25] F. Marabelli, G. B. Parravicini, and F. Salghetti-Drioli, *Phys. Rev. B* **52**, 1433 (1995).
- [26] M. Heinemann, B. Eifert, and C. Heiliger, *Phys. Rev. B* **87**, 115111 (2013).
- [27] See Supplemental Material at <http://link.aps.org/supplemental/10.1103/PhysRevB.99.075124> for more details about XPD calculations, DFT+*U* results, and SE data.
- [28] G. van der Laan, C. Westra, C. Haas, and G. A. Sawatzky, *Phys. Rev. B* **23**, 4369 (1981).
- [29] F. J. Garcia de Abajo, M. A. Van Hove, and C. S. Fadley, *Phys. Rev. B* **63**, 075404 (2001).
- [30] D. Tahir and S. Tougaard, *J. Phys.: Condens. Matter B* **24**, 175002 (2012).
- [31] J. Ghijsen, L. H. Tjeng, J. van Elp, H. Eskes, J. Westerink, G. A. Sawatzky, and M. T. Czyzyk, *Phys. Rev. B* **38**, 11322 (1988).
- [32] J. Zaanen, G. A. Sawatzky, and J. W. Allen, *Phys. Rev. Lett.* **55**, 418 (1985).
- [33] M. Imada, A. Fujimori, and Y. Tokura, *Rev. Mod. Phys.* **70**, 1039 (1998).
- [34] H. Eskes, L. H. Tjeng, and G. A. Sawatzky, *Phys. Rev. B* **41**, 288 (1990).
- [35] F. Parmigiani and L. Sangaletti, *J. Electron Spectrosc. Relat. Phenom.* **107**, 49 (2000).
- [36] C. P. J. Adolphs, S. Moser, G. A. Sawatzky, and M. Berciu, *Phys. Rev. Lett.* **116**, 087002 (2016).
- [37] I. J. Hamad, L. O. Manuel, and A. A. Aligia, *Phys. Rev. Lett.* **120**, 177001 (2018).
- [38] D. E. Aspnes, *Optical Properties of Solids: New Developments*, edited by B. O. Seraphin (North Holland, Amsterdam, 1976), pp. 799–846.
- [39] G. E. Jellison and F. A. Modine, *Appl. Phys. Lett.* **69**, 371 (1996).
- [40] J. Tauc, R. Grigorovici, and A. Vancu, *Phys. Status Solidi B* **15**, 627 (1966).
- [41] F. P. Koffyberg and F. A. Benko, *J. Appl. Phys.* **53**, 1173 (1982).
- [42] D. Wu, Q. Zhang, and M. Tao, *Phys. Rev. B* **73**, 235206 (2006).
- [43] S. A. Chambers, T. Droubay, T. C. Kaspar, and M. Gutowski, *J. Vac. Sci. Technol. B* **22**, 2205 (2004).
- [44] A. Giampietri, G. Drera, I. Píř, E. Magnano, and L. Sangaletti, *Appl. Phys. Lett.* **109**, 132903 (2016).